ChemComm
Chemical Communications

Accepted Manuscript

This article can be cited before page numbers have been issued, to do this please use: S. T. Lee, C. Bailey, D. A. Santos, M. Bhadbhade, H. Kim and D. J. Kim, *Chem. Commun.*, 2026, DOI: 10.1039/D5CC05355B.

ROYAL SOCIETY OF CHEMISTRY

rsc.li/chemcomm

ChemComm

View Article Online
DOI: 10.1039/D5CC05355B

COMMUNICATION

Electronic Coupling in a Synthetic Model of the Cu–Cofactor Unit of the P_M State in Cytochrome *c* Oxidase

Received 00th January 20xx,
Accepted 00th January 20xx

DOI: 10.1039/x0xx00000x

Sang Tae Lee[a], Christopher G. Bailey[b, c], Daniel A. Santos[a], Mohan Bhadbhade[d], Heejin Kim[e*], and Dong Jun Kim[a*]

A hydroquinone–imidazole–Cu(II) complex reproduces the Tyr–His–Cu unit of cytochrome *c* oxidase. Laser-induced EPR and DFT reveal a semiquinone radical electronically isolated from Cu(II) by orthogonal orbital alignment. The weak magnetic exchange underscores how geometry governs coupling, providing insight into transient states of metalloenzymes and their synthetic analogues.

Energy conversion in biological systems is driven by orchestrated sequences of electron and proton transfer events. This process is driven by cytochrome *c* oxidase (C*c*O), the terminal respiratory enzyme that catalyses the four-electron reduction of dioxygen to water while translocating protons across a membrane. This dual function underlies the generation of the electrochemical gradient used for adenosine triphosphate synthesis, with C*c*O accounting for the majority of energy conserved through oxidative metabolism. At its core, the binuclear centre (BNC), comprising heme a_3 and Cu_B, coordinates redox transformations and proton pumping.[1-3]

Within the catalytic sequence, the P_M intermediate arises immediately following O–O bond cleavage, preceding proton transfer steps that yield water.[4-10] The histidine–tyrosine (His–Tyr) crosslink, first identified in crystallographic studies of bovine C*c*O, remains a distinctive feature of the active site.[1] A wide range of synthetic strategies have sought to reproduce this crosslink and explore its role in redox chemistry, yielding insights but often limited by instability.[11-27] Raman and crystallographic studies provided clear evidence for a ferryl–oxo Fe^{IV}=O unit accompanied by a Cu^{II} centre and a tyrosyl radical on the covalently crosslinked His–Tyr residue.[28, 29] This finding reframed the question of how the three redox-active sites—Fe^{IV}, Cu^{II}, and Tyr•—communicate electronically. Magnetic exchange between Cu^{II} and the tyrosyl radical within P_M has been the focus of significant recent progress. Computational modelling with spectroscopic interpretation by Schaefer and co-workers[30] suggested that the Cu–Tyr pair could exhibit ferromagnetic coupling under certain geometries. More recently, high-resolution magnetic circular dichroism measurements by José et al.[31] established that P_M is best described as a three-spin system, Fe^{IV}=O (S = 1), Cu^{II} (S = ½), and Tyr• (S = ½), with overall antiferromagnetic behaviour. Their analysis assigned specific pairwise couplings within this triad, including antiferromagnetic exchange between Cu and Tyr. However, because these couplings are defined in the context of the full Fe–Cu–Tyr system, the intrinsic Cu–Tyr interaction cannot be disentangled from Fe-mediated superexchange or protein-imposed geometry. This leaves open the question of how these two centres interact in isolation.

Here, we report a hydroquinone–imidazole–Cu(II) complex as a synthetic subunit analogue of the Tyr–His–Cu_B subunit in C*c*O that provides a platform for characterising the intrinsic electronic coupling between Cu(II) and the cofactor. Using laser-induced electron paramagnetic resonance (EPR) spectroscopy, we detect the formation of a stable semiquinone-radical coordinated to Cu(II), in a geometry that density functional theory (DFT) calculations indicate yields orthogonal spin densities, resulting in weak exchange. This

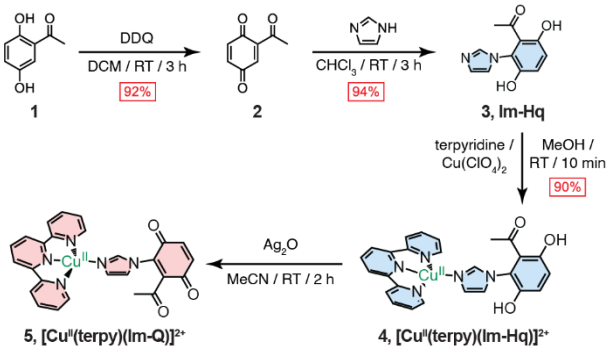

Fig. 1 Synthetic route to cofactor and Cu(II) complexes. Yields for each step are shown in red.

[a] School of Chemistry, University of New South Wales, Sydney, NSW 2052, Australia.
[b] School of Physics, The University of Sydney, Sydney, NSW 2006, Australia
[c] Sydney Nano, The University of Sydney, Sydney, NSW 2006, Australia
[d] Mark Wainwright Analytical Centre, University of New South Wales, Sydney, NSW 2052, Australia
[e] Research Center for Materials Analysis, Korea Basic Science Institute, Daejeon 34133, Republic of Korea

View Article Online
DOI: 10.1039/D5CC05355B

result aligns with earlier interpretations of minimal Cu–Tyr coupling in model systems[30], while complementing the three-spin topology determined in the intact P_M state.[31] By resolving the behaviour of the Cu–cofactor, this platform provides a mechanistic reference point for understanding how protein constraints modulate exchange in C*c*O.

Binding of O_2 to the reduced binuclear centre gives the oxy intermediate (A).[32-33] Subsequent O–O bond cleavage, driven by proton and electron transfer from the His–Tyr cross linked residue, produces the P_M state, formulated as an $Fe_{a3}(IV)=O$, $Cu_B(II)$–OH, TyrO• triad.[34] The computational study of Blomberg indicates that in this P_M state the TyrO• unit accepts electron density and carries substantial spin density in a phenoxyl like π system centred on the oxygen atom.[35] To capture this local electronic structure we use the Im–Hq/Im–Sq platform. Deprotonation and one electron oxidation of Im–Hq give an O centred semiquinone (Im–Sq) that behaves as a phenoxyl radical strongly coupled to Cu(II) through the imidazole–aryl framework, providing a synthetic model for the TyrO•–Cu_B(II) fragment in the P_M state.

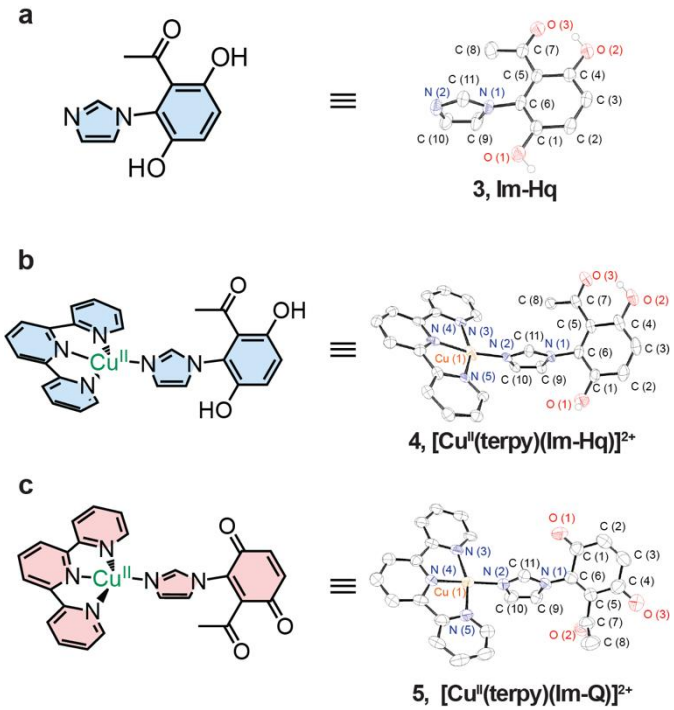

Fig. 2 a–c, The chemical structure (left) and single-crystal X-ray structure (right) of ligand **3, Im–Hq**, Cu(II) complex **4, [Cu^{II}(terpy)(Im-Hq)]$^{2+}$**, and oxidized Cu(II) complex **5, [Cu^{II}(terpy)(Im-Q)]$^{2+}$** are shown. All structures are depicted with thermal ellipsoids at the 50% probability level; hydrogen atoms and counterions are omitted for clarity. For cofactor **3**, selected bond distances (in Å) include N(1)–C(6) = 1.434, O(1)–C(1) = 1.352, and O(2)–C(4) = 1.353. For complex **4**, the bond distance N(1)–C(6) is 1.415, and the Cu–N distances range from 1.854 to 2.024 Å. In complex **5**, N(1)–C(6) measures 1.396 Å, and the Cu–N bond lengths range from 1.910 to 2.031 Å. The dihedral angle between the imidazole and quinol/quinone planes decreases progressively across the series, measured as 88.75° in **3**, 74.05° in **4**, and 48.19° in **5**.

Synthetic analogues of the His–Tyr cofactor have conventionally relied on phenol scaffolds to mimic the tyrosyl radical, yet these constructs are often limited by oxidative instability.[13, 30, 36-39] To overcome this, we employed a 2-acetyl-1,4-hydroquinone to generate an imidazole–hydroquinone **(Im-Hq)** ligand (Fig. S1). Coordination to Cu(II)–

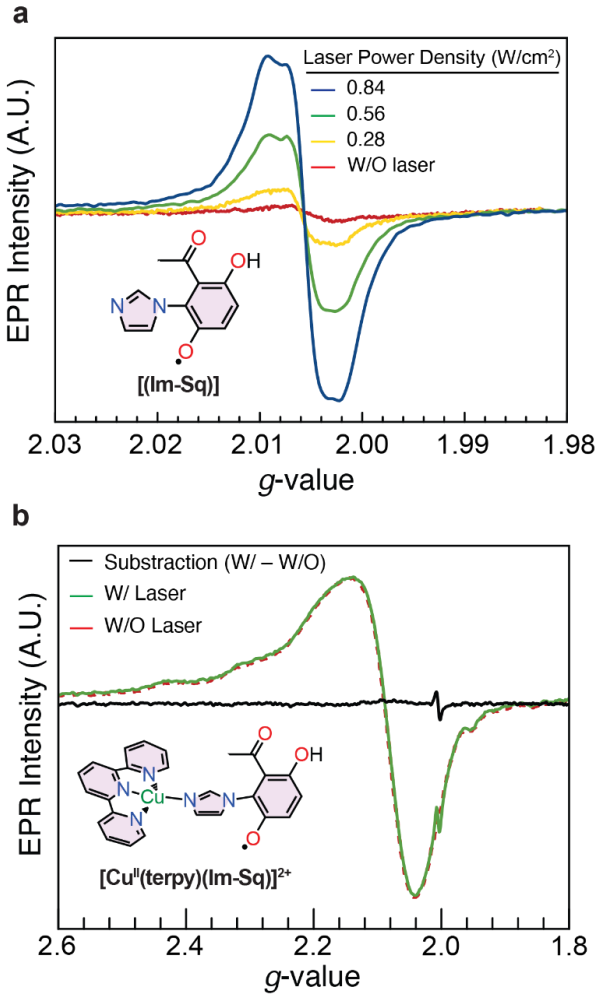

Fig. 3 a, EPR spectra of **(Im–Sq)** measured at 100 K in acetonitrile under laser irradiation at varying power densities: 0.28 W/cm² (3.6 mJ), 0.56 W/cm² (7.2 mJ), and 0.84 W/cm² (10.8 mJ). Spectra collected in the absence of laser irradiation (W/O laser) are also included for comparison. b, Corresponding spectra for **[Cu^{II}(terpy)(Im–Sq)]$^{2+}$** collected under identical conditions, displaying the spectrum with laser irradiation (green), without laser (red), and the subtracted difference (black).

terpyridine afforded **[Cu^{II}(terpy)(Im-Hq)]$^{2+}$**, with in situ oxidation yielding the quinone analogue **[Cu^{II}(terpy)(Im-Q)]$^{2+}$** (Fig. 1). Yields and characterisation data are provided in the Supplementary Information.

View Article Online
DOI: 10.1039/D5CC05355B

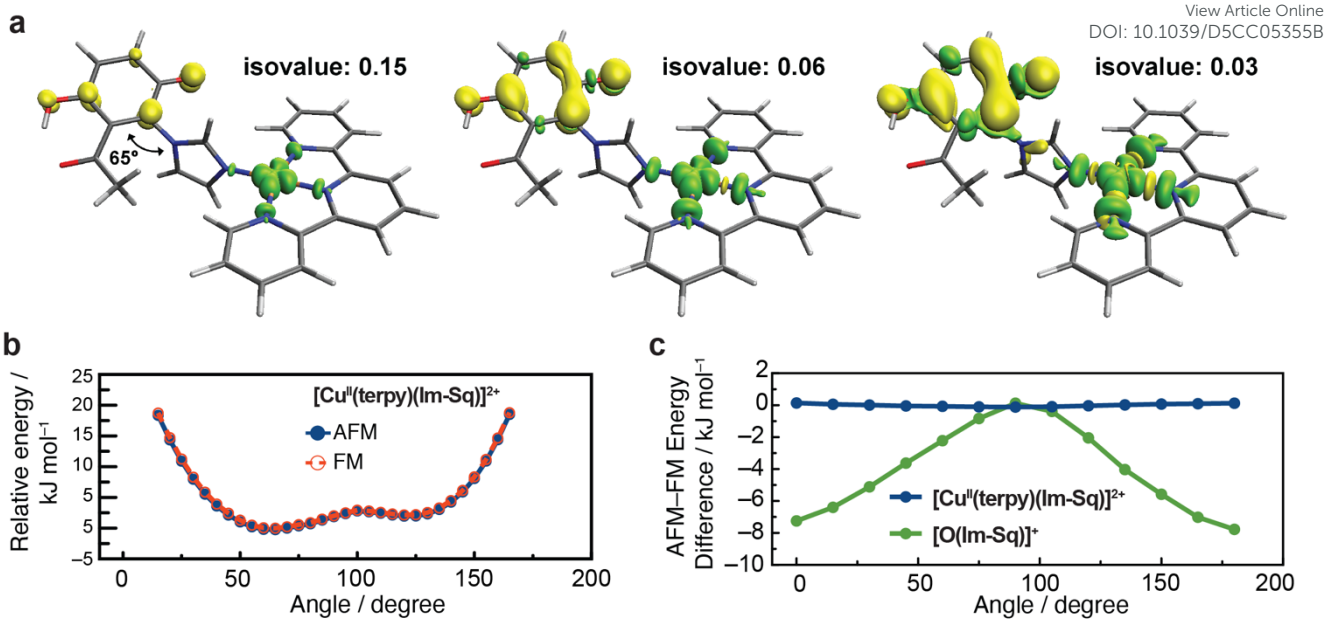

Fig. 4 a, Spin density isosurfaces of the antiferromagnetic state at a torsional angle of 65°, displayed at isovalues of 0.15, 0.06, and 0.03. Blue, red, grey, and white bars represent N, O, C, and H atoms, respectively. Green and yellow surfaces indicate excess up and down spin density, respectively. b, Relative electronic energies of the AFM and FM states, referenced to the minimum for each spin state, plotted as a function of torsion angle. c, AFM–FM energy difference ($\Delta E = E_{AFM} - E_{FM}$) as a function of angle for **[Cu^{II}(terpy)(Im–Sq)]$^{2+}$** (blue) and **[O-(Im-Sq)]$^{+}$** (green).

Single-crystal X-ray diffraction of **Im-Hq**, **[Cu^{II}(terpy)(Im-Hq)]$^{2+}$**, and **[Cu^{II}(terpy)(Im-Q)]$^{2+}$** revealed a progressive geometric evolution across the redox series (Fig. 2). Oxidation of the hydroquinone to quinone was marked by C–O bond contraction (1.360 → 1.206 Å), shortening of the N(imidazole)–C bond (1.415 → 1.396 Å), and elongation of the Cu–N(imidazole) bond (1.854 → 1.967 Å). The most notable trend was in the dihedral angle between the aromatic and imidazole planes, decreasing from 88.7° in the free ligand to 74.0° in **[Cu^{II}(terpy)(Im-Hq)]$^{2+}$** and 48.2° in **[Cu^{II}(terpy)(Im-Q)]$^{2+}$**. This systematic reduction highlights how redox chemistry reorganises the geometry of this motif, potentially underpinning conformational control in the native His–Tyr crosslink of CcO. As dihedral angle directly governs orbital overlap, it provides a quantifiable parameter linking redox events to electronic coupling and frames the interpretation of subsequent EPR studies.

In order to probe radical formation and the electronic structure for **[Cu^{II}(terpy)(Im-Hq)]$^{2+}$** and its oxidised analogue **[Cu^{II}(terpy)(Im–Sq)]$^{2+}$**, we performed EPR spectroscopy under laser excitation. Triethylamine (3 equiv.) was added prior to measurement to facilitate semiquinone generation at 100 K without inducing full deprotonation. UV–vis spectra recorded before and after triethylamine addition showed no significant shift (Fig. S2), confirming that the hydroquinone remains protonated under ambient conditions. Samples were flash-frozen in liquid nitrogen and analysed by EPR at 100 K under variable laser excitation. The quinone complex, **[Cu^{II}(terpy)(Im-Q)]$^{2+}$** (**5**), is used only to establish the redox-dependent structural trend and is not an intermediate in the laser-induced generation of the semiquinone radical.

Laser-irradiated EPR spectra of **Im-Hq** (Fig. 3a) reveal the formation of a semiquinone-radical, with a g-value of 2.0057, characteristic of a phenoxyl-type radical localised near the oxygen atom. This value lies within the range reported for tyrosyl radicals (g ≈ 2.005 – 2.0058) and suggests that the spin density remains largely confined to the aromatic ring system.[40] The electronic structure inferred from this g-value is consistent with a scenario in which the unpaired electron is localised within the semiquinone π-system with minimal delocalisation onto adjacent groups. As will be discussed in the DFT section below, this localisation likely arises from a twisted geometry between the semiquinone and imidazole rings, limiting π-conjugation and orbital overlap.

In the **[Cu^{II}(terpy)(Im-Hq)]$^{2+}$** complex (Fig. 3b), the EPR spectra features characteristic of an elongated octahedral-square pyramidal Cu(II) coordination environment.[41] Upon laser excitation, a new radical signal with g = 2.0050 emerges, while the Cu(II) peak ($g_{||}$ = 2.26, $g_{\perp}$ = 2.08) remains unaltered. Subtraction of the pre-excitation spectrum confirms independent generation of the radical signal. The slightly lower g-value compared to the free cofactor reflects subtle differences in the local environment, but the absence of major spectral changes indicates minimal spin delocalisation into the ligand or metal orbitals. Spectral simulations using EasySpin yielded comparable fits for both ferromagnetic (FM) and antiferromagnetic (AFM) coupling models, indicating the exchange interaction near the resolution limit of the technique.

To further examine the electronic arrangement, we performed DFT calculations on the semiquinone–imidazole–Cu(II) (**[Cu^{II}(terpy)(Im-Sq)]$^{2+}$**) complex, incorporating acetonitrile as the solvent. Spin density maps in Fig. 4a visualised at different isovalues of 0.15, 0.06, and 0.03, together spin population analysis (Fig. S3), reveal that the up-spin density is concentrated on the Cu(II) centre and its four planar nitrogen ligands, while the down-spin density is largely confined to the π-system of the semiquinone. It indicates that both the Cu(II) and semiquinone centres have weak spin interactions with the bridging imidazole. The spin communication between Cu(II)

and the imidazole ligand occurs through σ-type interactions between Cu(II) $dx^2–y^2$ orbital and the lone pair of the imidazole nitrogen. These specific orbitals are orthogonal to the π-system, which in turn restricts spin interaction between the Cu(II) and imidazole. On the other hand, between the semiquinone and imidazole ligand, the spin localisation is associated with a twisted geometry (dihedral angle ~65°) between their planes, which limits π-overlap and through-space conjugation. These spin and geometry arrangements yield a weak spin coupling between the Cu(II) and semiquinone centres, consistent with the EPR observations.

DFT scans of the dihedral angle between the semiquinone and imidazole support the above interpretation. When rotating the angle (Fig. 4b), the spin interaction between the two moieties varies, but the aforementioned orbital orthogonality between the Cu(II) and imidazole restricts the spin coupling over the entire complex. This leads to only ~0.2 kJ mol^{-1} energy difference between AFM and FM states across the range (black line in Fig. 4c). To examine the impact of the dihedral angle, we next explored a system in which Cu(II) was replaced by an oxygen-centred radical (Fig S4), i.e., **[O-(Im-Sq)]**$^+$, as the O$^\bullet$ has an excess electron in p-orbital and can make π-overlap with the imidazole depending on a dihedral angle. In a sharp contrast to the **[Cu^{II}(terpy)(Im-Sq)]**$^{2+}$ case, **[O-(Im-Sq)]**$^+$ system exhibits a strong angle-dependent energy profile. The energy difference between AFM and FM states is ~8 kJ mol^{-1} (green line in Fig. 4c) at two endpoints, where the π-systems are aligned, while it approaches zero at orthogonal geometries (around 90°), where orbital overlap is suppressed. This result confirms that the dihedral angle primarily acts as a structural gate that keeps the spin coupling weak. In the protein context, modest conformational changes at the His–Tyr motif could therefore modulate proton-coupled electron transfer at the P_M state without altering the underlying oxidation states of the metals and cofactor. In this light, the His–Tyr motif in C*c*O may function as a conformationally regulated electron–proton transfer gateway. Together with the EPR results, these findings demonstrate that orthogonal orbital symmetry electronically isolates the Cu(II)–cofactor pair, providing a subunit-level complement to the three-spin topology of P_M.

In summary, we have developed a hydroquinone–imidazole–Cu(II) complex as a structurally defined analogue of the Tyr–His–Cu subunit in C*c*O. Structural analysis revealed redox-dependent flattening of the ligand framework, while laser-induced EPR and DFT studies demonstrated that the semiquinone radical and Cu(II) centre remain electronically decoupled by orthogonal orbital alignment. The small AFM–FM energy differences (<0.2 kJ mol^{-1}) underscore the intrinsically weak magnetic exchange within this Cu–cofactor pair. These findings provide a subunit-level perspective that complements multi-spin descriptions of the P_M state and highlight dihedral angle and orbital orientation as design parameters for controlling coupling in redox cofactors. Beyond enzymatic modelling, this approach offers opportunities to control spin topology, enabling architecturally programmed proton-coupled electron transfer in responsive, bioinspired systems.

The authors acknowledge support from the Australian Research Council (DE210101618) and the Korea Basic Science Institute (C512310).

Conflicts of interest

There are no conflicts to declare.

Data availability

The data supporting this study are available in the Supporting Information of this article. Supplementary crystallographic data are available from the CCDC under deposition numbers 2432274 (**3**), 2432390 (**4**), and 2432275 (**5**).

Notes and references

1 S. Yoshikawa, K. Shinzawa-Itoh, R. Nakashima, R. Yaono, E. Yamashita, N. Inoue, M. Yao, M. J. Fei, C. P. Libeu, T. Mizushima, H. Yamaguchi, T. Tomizaki and T. Tsukihara, *Science*, 1998, **280**, 1723-1729.

2 C. Ostermeier, A. Harrenga, U. Ermler and H. Michel, *Proc. Nat. Ac. Sci.*, 1997, **94**, 10547-10553.

3. T. Soulimane, G. Buse, G. P. Bourenkov, H. D. Bartunik, R. Huber and M. E. Than, *EMBO J.*, 2000, **19**, 1766-1776-1776.

4. A. Shimada, T. Tsukihara and S. Yoshikawa, *Front. Chem.*, 2023, **11**. doi:10.3389/fchem.2023.1108190

5. I. Ishigami, R. G. Sierra, Z. Su, A. Peck, C. Wang, F. Poitevin, S. Lisova, B. Hayes, F. R. Moss, S. Boutet, R. E. Sublett, C. H. Yoon, S.-R. Yeh and D. L. Rousseau, *Nat. Comm.*, 2023, **14**, 5752.

6. M. Wikström and V. Sharma, *Biochim. Biophys. Acta*, 2018, **1859**, 692-698.

7. F. Kolbe, S. Safarian, Ż. Piórek, S. Welsch, H. Müller and H. Michel, *Nat. Comm.*, 2021, **12**, 6903.

8. D. L. Rousseau, I. Ishigami and S.-R. Yeh, *J. Inorg. Biochem.*, 2025, **262**, 112730.

9. R. Paduvari, R. Arekal and D. M. Somashekara, *Int. J. Biol. Macromol.*, 2025, **309**, 142773.

10. V. Sharma, K. D. Karlin and M. Wikström, *Proc. Nat. Ac. Sci.*, 2013, **110**, 16844-16849.

11. D. G. Lonnon, S. T. Lee and S. B. Colbran, *J. Am. Chem. Soc.*, 2007, **129**, 5800-5801.

12. J.-G. Liu, Y. Naruta and F. Tani, *Chem.–Eur. J.*, 2007, **13**, 6365-6378.

13. J. P. Collman, N. K. Devaraj, R. A. Decréau, Y. Yang, Y.-L. Yan, W. Ebina, T. A. Eberspacher and C. E. D. Chidsey, *Science*, 2007, **315**, 1565-1568.

14. J. P. Collman, R. A. Decréau, Y. Yan, J. Yoon and E. I. Solomon, *J. Am. Chem. Soc.*, 2007, **129**, 5794-5795.

15. J.-G. Liu, Y. Naruta, F. Tani, T. Chishiro and Y. Tachi, *Chem. Commun.*, 2004, **1**, 120-121.

16. K. Kamaraj, E. Kim, B. Galliker, L. N. Zakharov, A. L. Rheingold, A. D. Zuberbühler and K. D. Karlin, *J. Am. Chem. Soc.*, 2003, **125**, 6028-6029.

17. J. A. Cappuccio, I. Ayala, G. I. Elliott, I. Szundi, J. Lewis, J. P. Konopelski, B. A. Barry and Ó. Einarsdóttir, *J. Am. Chem. Soc.*, 2002, **124**, 1750-1760.

18. K. M. McCauley, J. M. Vrtis, J. Dupont and W. A. van der Donk, *J. Am. Chem. Soc.*, 2000, **122**, 2403-2404.

View Article Online
DOI: 10.1039/D5CC05355B

19. J. P. Collman, Z. Wang, M. Zhong and L. Zeng, *J. Chem. Soc., Perkin Trans. 1*, 2000, **8,** 1217-1222.
20. M. Aki, T. Ogura, Y. Naruta, T. H. Le, T. Sato and T. Kitagawa, *The J. Phys. Chem. A*, 2002, **106**, 3436-3444.
21. M. Voicescu, Y. El Khoury, D. Martel, M. Heinrich and P. Hellwig, *J. Phys. Chem. B*, 2009, **113**, 13429-13436.
22. F. Himo, L. Noodleman, M. R. A. Blomberg and P. E. M. Siegbahn, *J. Phys. Chem. A*, 2002, **106**, 8757-8761.
23. R. P. Pesavento, D. A. Pratt, J. Jeffers and W. A. van der Donk, *Dalton T.*, 2006, **27,** 3326-3337.
24. S. B. Colbran and M. N. Paddon-Row, *J. Biol. Inorg. Chem.*, 2003, **8**, 855-865.
25. Z. He, S. B. Colbran and D. C. Craig, *Chem.–Eur. J.*, 2003, **9**, 116-129.
26. J. P. Collman, R. A. Decréau and C. J. Sunderland, *Chem. Commun.*, 2006, **37,** 3894-3896.
27. K. D. Karlin and E. Kim, *Chem. Lett.*, 2004, **33**, 1226-1231.
28. I. Ishigami, A. Lewis-Ballester, A. Echelmeier, G. Brehm, N. A. Zatsepin, T. D. Grant, J. D. Coe, S. Lisova, G. Nelson, S. Zhang, Z. F. Dobson, S. Boutet, R. G. Sierra, A. Batyuk, P. Fromme, R. Fromme, J. C. H. Spence, A. Ros, S.-R. Yeh and D. L. Rousseau, *Proc. Nat. Ac. Sci.*, 2019, **116**, 3572-3577.
29. K. Oda, T. Ogura, E. H. Appelman and S. Yoshikawa, *FEBS Lett.*, 2004, **570**, 161-165.
30. A. W. Schaefer, A. C. Roveda, Jr., A. Jose and E. I. Solomon, *J. Am. Chem. Soc.*, 2019, **141**, 10068-10081.
31. A. Jose, A. W. Schaefer, A. C. Roveda, W. J. Transue, S. K. Choi, Z. Ding, R. B. Gennis and E. I. Solomon, *Science*, 2021, **373**, 1225-1229.
32. M. I. Verkhovsky, J. E. Morgan and M. Wikstroem, Biochemistry, 1994, **33**, 3079–3086.
33. A. Sucheta, I. Szundi and Ó. Einarsdóttir, Biochemistry, 1998, **37**, 17905–17914.
34. M. Karpefors, P. Ädelroth, A. Namslauer, Y. Zhen and P. Brzezinski, Biochemistry, 2000, **39**, 14664–14669.
35. M. R. A. Blomberg, Biochemistry, 2016, **55**, 489–500.
36. A. Offenbacher, K. N. White, I. Sen, A. G. Oliver, J. P. Konopelski, B. A. Barry and Ó. Einarsdóttir, *J. Phys. Chem. B*, 2009, **113**, 7407-7417.
37. Y. Nagano, J.-G. Liu, Y. Naruta, T. Ikoma, S. Tero-Kubota and T. Kitagawa, *J. Am. Chem. Soc.*, 2006, **128**, 14560-14570.
38. D. A. Proshlyakov, M. A. Pressler and G. T. Babcock, *Proc. Nat. Ac. Sci.*, 1998, **95**, 8020-8025.
39. K. N. White, I. Sen, I. Szundi, Y. R. Landaverry, L. E. Bria, J. P. Konopelski, M. M. Olmstead and Ó. Einarsdóttir, *Chem. Commun.*, 2007, **31**, 3252-3254.
40. E. Kim, E. E. Chufán, K. Kamaraj and K. D. Karlin, *Chem. Rev.*, 2004, **104**, 1077-1134.
41. C.-C. Su and C.-B. Li, *Polyhedron*, 1994, **13**, 825-834.

View Article Online
DOI: 10.1039/D5CC05355B

The data supporting this article have been included as part of the Supplementary Information. Supplementary crystallographic data are available from the CCDC under deposition numbers 2432274 (3), 2432390 (4), and 2432275 (5).